

The CFD Investigation of Airframe Components and their Interactions on Aerodynamics Characteristics of Unmanned Aerial Vehicle (UAV)

Artit Ridluan^{1*} Anotai Suksangpanomrung² Pongjet Promvong³

¹Research and Development Center, Summit Auto Seat Industry Ltd, Samut Prakan, 10540

²Department of Mechanical Engineering, Academic Division, Chulachomklao Royal Military Academy, Nakorn-Nayok, 26001.

³Department of Mechanical Engineering, Faculty of Engineering, King Mongkut's Institute of Technology Ladkrabang, Ladkrabang, Bangkok 10520.

*E-mail: aridluan@yahoo.com, asuksang@crma.ac.th, ktongje@kmitl.ac.th

Abstract

Computational Fluid Dynamics (CFD) was utilized as the investigating tool to study and describe the influences of UAV components and their interactions, composed of the NACA652-415 wing, fuselage, and v-tail, on the aerodynamic features.

The computation of flow over UAV geometries with the angle of attack, ranging from -4 to 16 degrees, was exhibited at Reynolds Number of 3×10^6 . The investigation was focused mainly on the behavior of lift and drag coefficients of the wing since they are the important parameters to develop and improve a more efficient aircraft.

To validate the numerical accuracy on the chosen models, the viscous hybrid mesh was used as the CFD experimental reference. The calculation with viscous hybrid mesh yielded increasing of drag coefficients and decreasing of lift coefficients.

The CFD results revealed that the wing-fuselage interaction caused of the slightly steeper slope of lift coefficient and the lower drag coefficient as well as the shift of the stalling point from 13 to 15 degrees. Comparative to the wing-fuselage configuration, the tail installation resulted in the slightly lower lift and drag coefficients. Aside from quantification, the highly three dimensional and large separation flow regime was strongly dominated at the incidence beyond the stall angle, resulting in the drop of the lift coefficients. In addition, the physics of the wing tip vortices was delineated.

Keywords: Aerodynamics, Unmanned Aerial Vehicle (UAV), Lift, Drag.

Introduction

Traditionally, investigating the aerodynamic performance of aircrafts was performed on the consideration of two-dimensional wings. Although the two-dimensional analysis can provide the beneficial

trends of predicting aerodynamic qualities, however, the significant flow physics of the actual aircraft are eliminated.

Even though the researches [1,2,3,4] on the complete aircrafts have been investigated. The influences of component interactions on aerodynamic parameters are still doubtful and unclear.

As the part of the airframe design and construction of the unmanned aerial vehicle (UAV) group, our research team would like to study insight into the aerodynamics of the UAV components and their interactions, including the wing, fuselage, and tail, as well as to predict all aerodynamic forces. Therefore, our objectives are to investigate and describe the flow mechanisms as well as drag and lift generation mechanisms of UAV components and their interactions with various angles of attack.

The research work was organized as follows. After the governing equations and corresponding models had been described, the UAV model and numerical simulations were discussed. Consequently, both qualitative and quantitative results were brought together to describe the flow fields on each component and their interaction between components. Finally, all of the results would be concluded and suggestions were made for future investigation.

1. Mathematical Models

To describe the turbulent phenomenon, the modification of Navier-Stokes equations (NSEs) was established by the Reynolds averaging method. The modified NSEs, called Reynolds-Averaged Navier-Stokes (RANS) equations. Both the continuity and RANS equations in conservation form are written in equation (1) and (2).

The Continuity equation:

$$\frac{\partial \rho}{\partial t} + \frac{\partial(\rho \cdot u_i)}{\partial x_i} = 0 \quad (1)$$

The RANS equations:

$$\begin{aligned} & \frac{\partial(\rho \cdot u_i)}{\partial t} + \frac{\partial(\rho \cdot u_i \cdot u_j)}{\partial x_j} \\ &= -\frac{\partial p}{\partial x_i} + \frac{\partial}{\partial x_j} \left[\mu \cdot \left(\frac{\partial u_i}{\partial x_j} + \frac{\partial u_j}{\partial x_i} - \frac{2}{3} \cdot \delta_{ij} \cdot \frac{\partial u_l}{\partial x_l} \right) \right] + \tau_{ij} \end{aligned} \quad (2)$$

Boussinesq Hypothesis

In equation (2) an additional stresses term or the Reynolds stresses are occurred. The common fashion, used to model the Reynolds Stress term, employs Boussinesq hypothesis relating the Reynolds stress with the velocity gradients as followed,

$$\tau_{ij} = \mu_t \cdot \left(\frac{\partial u_i}{\partial x_j} + \frac{\partial u_j}{\partial x_i} \right) - \frac{2}{3} \cdot \left(\rho \cdot k + \mu_t \cdot \frac{\partial u_l}{\partial x_l} \right) \cdot \delta_{ij} \quad (3)$$

Modeling turbulent eddy viscosity

The effect of turbulent eddy motions was described and presented through the turbulent viscosity term (μ_t). Accordingly, the appropriate closure model for μ_t is desirable. Owing to the superior capacity of the standard $k-\omega$ and $k-\varepsilon$ models, the Shear Stress Transport (SST) $k-\omega$ turbulent closure model was selected to describe the turbulent motions in this research. The eddy viscosity is related as follows.

$$\mu_t = \rho \cdot \frac{k}{\omega} \cdot \frac{1}{\max \left[\frac{1}{\alpha^*}, \frac{\Omega \cdot F_2}{a_1 \cdot \omega} \right]} \quad (4)$$

where the mean rate of rotation Ω is written in the form of the mean rate of rotation tensor, i.e.,

$$\Omega = \sqrt{2 \cdot \Omega_{ij} \cdot \Omega_{ij}}$$

and the blending function F_2 is defined as,

$$F_2 = \tanh(\Phi_2^2)$$

$$\Phi_2 = \max \left[2 \cdot \frac{\sqrt{k}}{0.09 \cdot \omega \cdot y}, \frac{500 \cdot \mu}{\rho \cdot y^2 \cdot \omega} \right]$$

and α^* is given by,

$$\alpha^* = \alpha^* \cdot \left(\frac{\alpha_0^* + Re_t / R_k}{1 + Re_t / R_k} \right)$$

Finally, the parameter Re_t and constant R_k and α_0^* are defined as,

$$Re_t = \frac{\rho \cdot k}{\mu \cdot \omega}$$

$$R_k = 6$$

$$\alpha_0^* = \frac{\beta_1}{3}, \beta_1 = 0.072.$$

The $k-\omega$ transport equations

The equations used to model the complex flow behaviors of the turbulent flow were k and ω equations and described as follows.

The k equations:

$$\frac{D(\rho \cdot k)}{Dt} = \frac{\partial}{\partial x_j} \left(\Gamma_k \cdot \frac{\partial k}{\partial x_j} \right) + G_k - Y_k + S_k \quad (5)$$

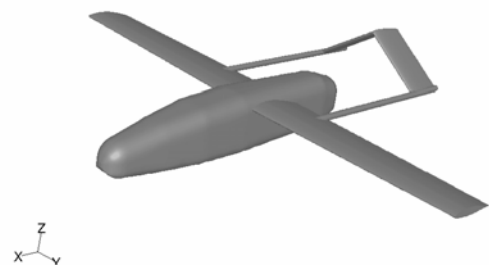
The ω equations:

$$\frac{D(\rho \cdot \omega)}{Dt} = \frac{\partial}{\partial x_j} \left(\Gamma_\omega \cdot \frac{\partial \omega}{\partial x_j} \right) + G_\omega - Y_\omega + D_\omega + S_\omega \quad (6)$$

Futher details of the $k-\omega$ transport equation can be found in [5].

2. UAV Configurations and CFD Methods

The commercial CFD code, Fluent 6.0, was used as a tool to predict the aerodynamic quantity of the designed UAV configurations. The models, used in this investigation, are presented in Figure 1 (a) for the wing-fuselage and tail and in Figure 1 (b) for the wing-fuselage.



(a)

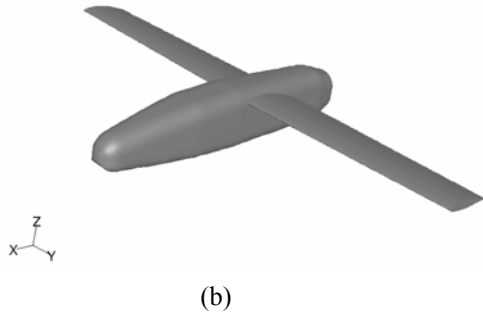


Figure 1. The geometries of UAV model (a) model 1 (b) model 2

The time-independent incompressible Navier-Stokes equations with the SST $k-\omega$ turbulent model were discretized using the finite volume method. QUICK and central differencing flow numerical schemes were applied for convective and diffusive terms, respectively. The discrete nonlinear equations were implemented implicitly. To enforce the mass conservation and evaluate the pressure field, the pressure-velocity coupling algorithm SIMPLE (Semi Implicit Method for Pressure-Linked Equations) was selected. The linearized equations were solved using multigrid method. Due to the geometrical complexity of UAV, the numerically approximated equations were performed on the collocated tetrahedral grid, comprising the approximately total cells of 500,000 for model 1 and 700,000 for model 2, both are shown in Figure 2 and 3.

The boundary conditions, used in the research, were as followed. The inlet condition was a uniform velocity profile, simulating the normal cruising condition of the mach number 0.27. The outlet was a pressure constant. Due to the symmetry of the flow along the longitudinal direction, the computational was calculated only half of the model with the symmetry condition.

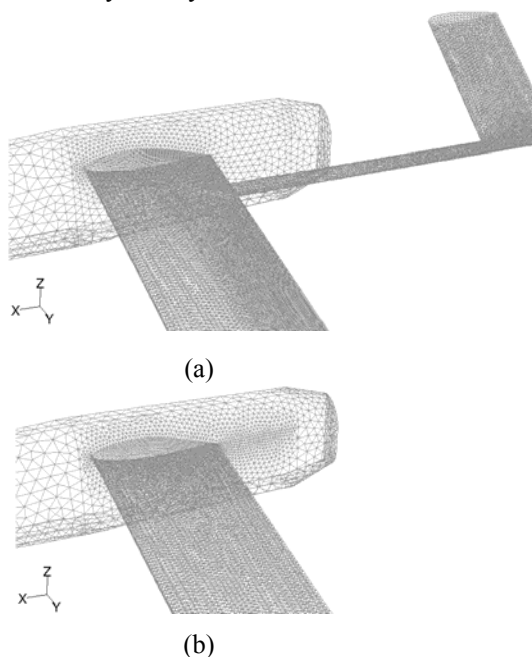


Figure 2. The surface grid distribution (a) model 1 (b) model 2

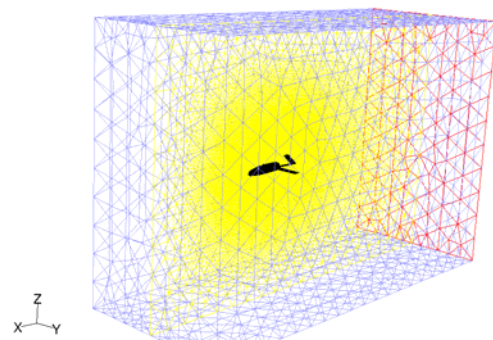


Figure 3. The grid distribution for the computational Domain

3. Results and Discussions

In the present investigation, the validation on both models with CFD was initially discussed and then, it was followed by the aerodynamics characteristics of the UAV components and their interactions and the flow dynamics.

3.1 CFD Validation

The viscous hybrid unstructured mesh with $k-\omega$ turbulent models was used to access the CFD accuracy of the chosen models. For the viscous hybrid grid, the prismatic volumes are generated in the boundary layer region. For the outer region, the tetrahedral cells were applied. To ensure the resolution of the surface, the average y^+ was approximately 5.

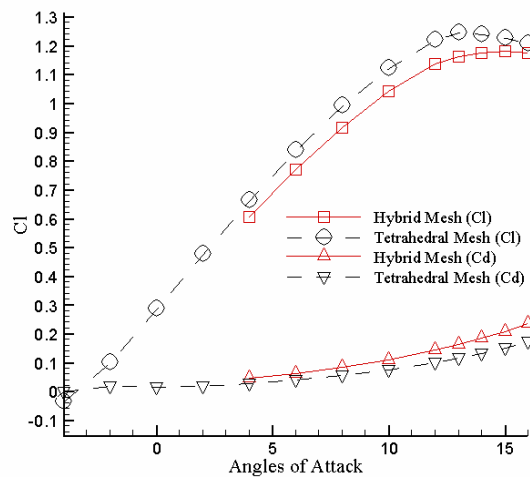


Figure 4. The comparisons of aerodynamic loads

It is obviously noticed that by using the tetrahedrons, drag coefficient (Cd) values are lower than those of the hybrid mesh, while in the case of lift coefficient (Cl) calculation, the hybrid mesh yields the lower values. Increasing of Cd and decreasing of Cl by the calculation using the viscous hybrid mesh are ascribed to the

resolution of boundary layer on the wing surfaces. The thickness of the boundary layer in the hybrid mesh plays the significant parameter for aerodynamic force calculation.

Although the boundary layer was not resolved, the ability to predict the aerodynamic forces of the tetrahedral mesh was not much different from the values of the viscous-hybrid mesh. Therefore, due to the computational resource restriction, the three-dimensional calculation of UAV would be performed using the tetrahedrons.

3.2 The Aerodynamics Characteristics

Obviously shown in Figure 5, C_l is linearly grown from -4 to 10 degrees. Afterward, the nonlinear behavior is found, corresponding to the appearance of flow separation, whereas the parabolic-like nonlinear characteristic is dominated for C_d values, although the attached flow is occupied throughout the wing surfaces. The minimum C_d is located at the -2 degree of incidence for all cases.

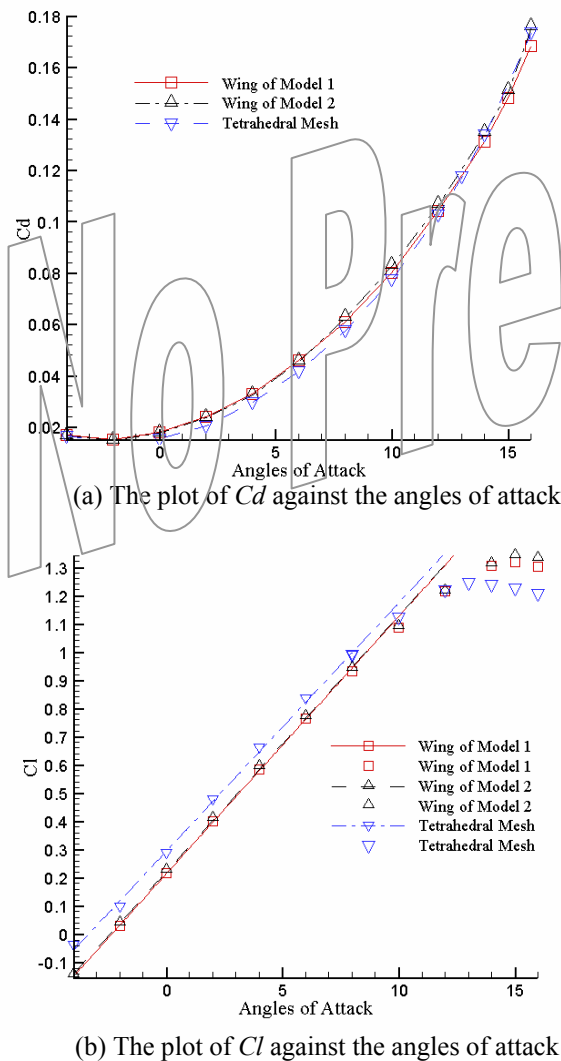
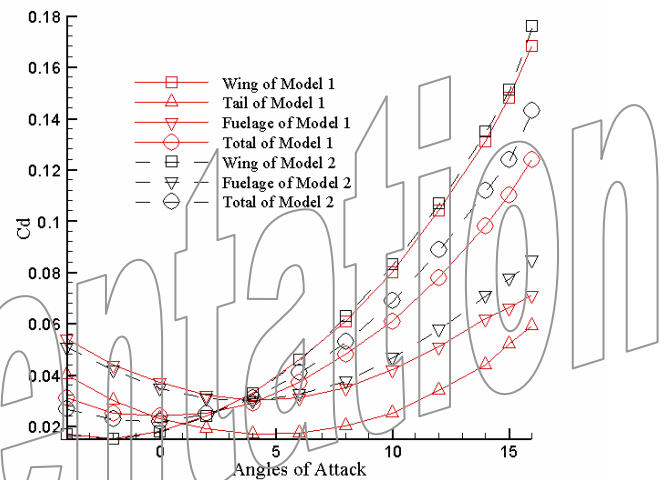


Figure 5. The influences of the component interactions on the aerodynamic loads (a) The plot of C_d against the

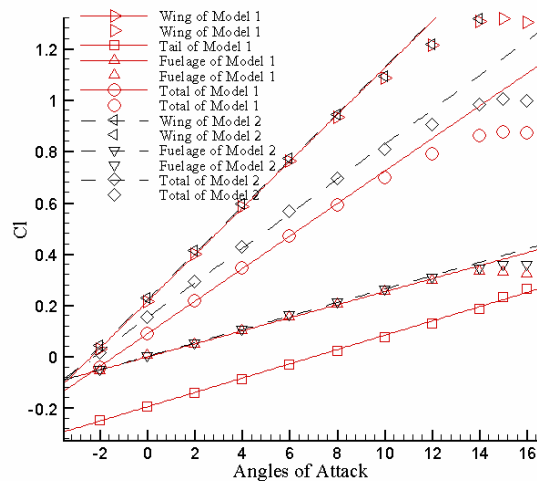
angles of attack and (b) The plot of C_l against the angles of attack

As depicted in Figure 5, the 3-D wing (tetrahedral mesh) provides the higher lift coefficients in the linear range, comparative to model 1 and model 2. After the 12 degree of angle of attack, the C_l values of model 1 and model 2 become more than those of the 3-D wing.

The differences of drag coefficients between model 1 and model 2 are clearly observed after the 6 degree of incidence. Unlike the values of lift coefficient, the drag coefficients of model 1 and model 2 are greater than those of 3-D wing at the incidence below 12 degree.



(a) The plot of C_d against the angles of attack



(b) The plot of C_l against the angles of attack

Figure 6. The decomposition of aerodynamic loads of UAV components (a) The plot of C_d against the angles of attack and (b) The plot of C_l against the angles of attack

As shown in Figure 6, the C_l and C_d behaviors of all components are similar. The slope of C_l of wing component is the steepest. The minimum drag coefficient

of tail and fuselage are at the 4 degree of incidence, while the minimum of the other is found at -2 degree of incidence. Since the large wake flow covered the fuselage, the lift coefficients of fuselage become nonlinear after 12 degree of incidence. For the tail, the separation regime was not appeared. Accordingly, there is no drop of the lift coefficient for the tail component.

The consideration of tail-installation influence by streamwise distribution of pressure coefficients on the wing surface, shown in Figure 7, is discussed. It is obviously seen that, after the leading edge, the pressures of the upper wing surface are step by step recovered and those of the lower surface are decreased. The upper-side pressures of the model 2 are less than the pressure of model 1, whereas the lower-side pressures of the model 2 are more than the pressure of model 1.

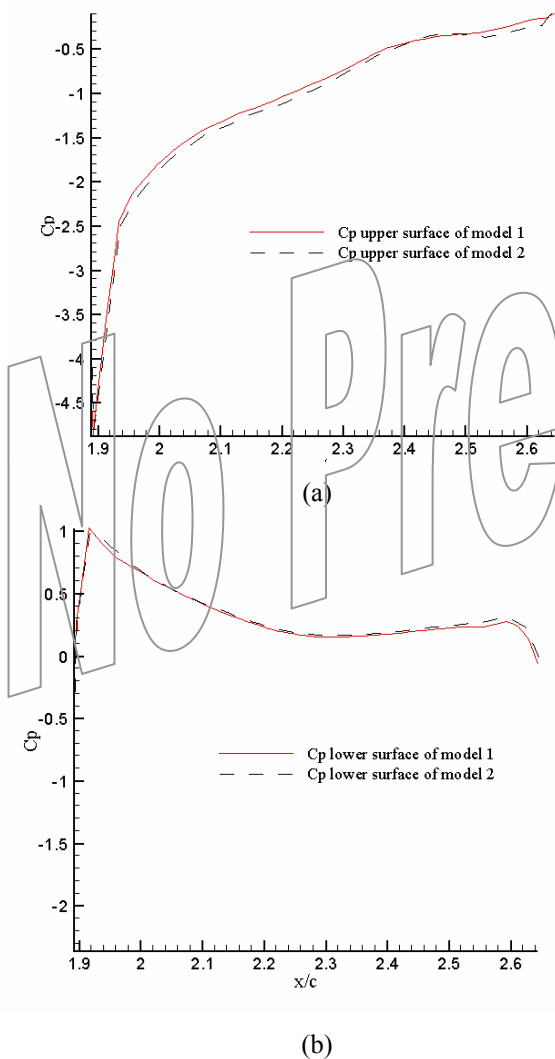
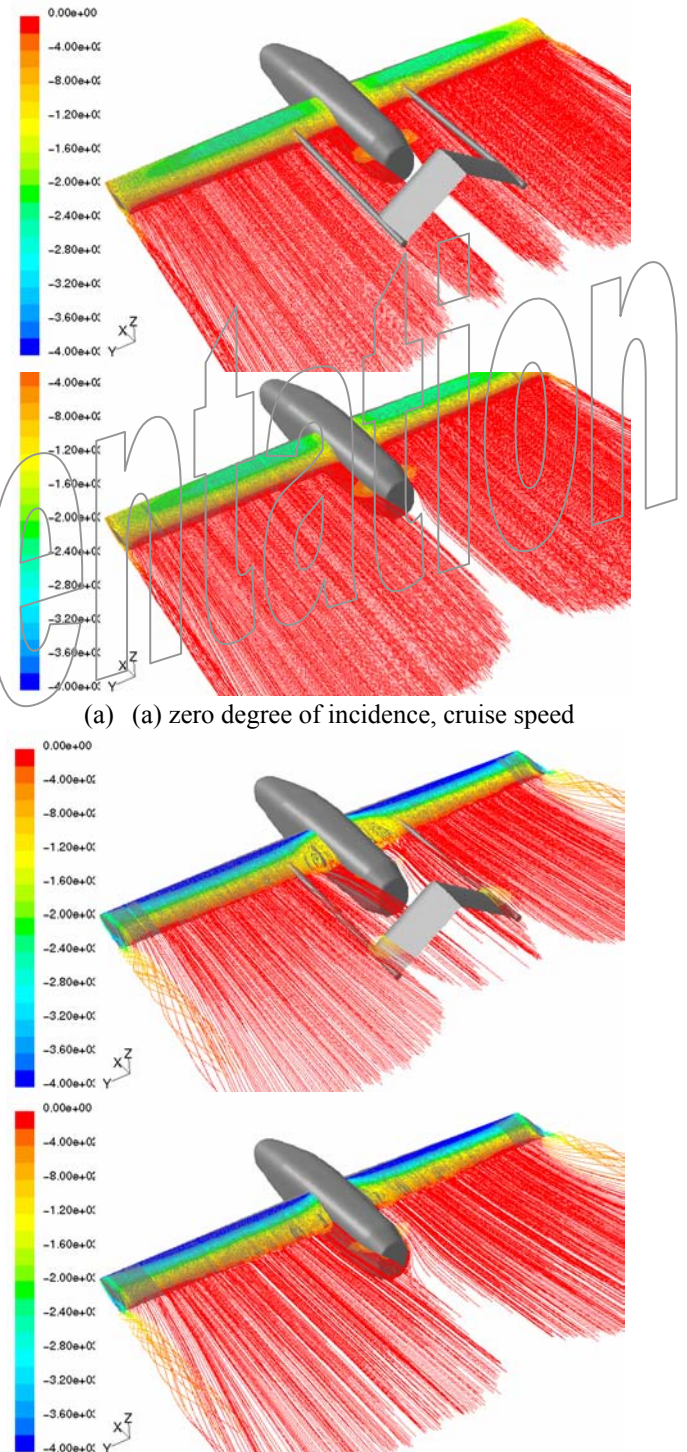


Figure 7 The plot of pressure coefficients along the x axis at 15 degree of incidence (a) upper surface at $y = 0.76$, and (b) lower surface at $y = 0.76$.

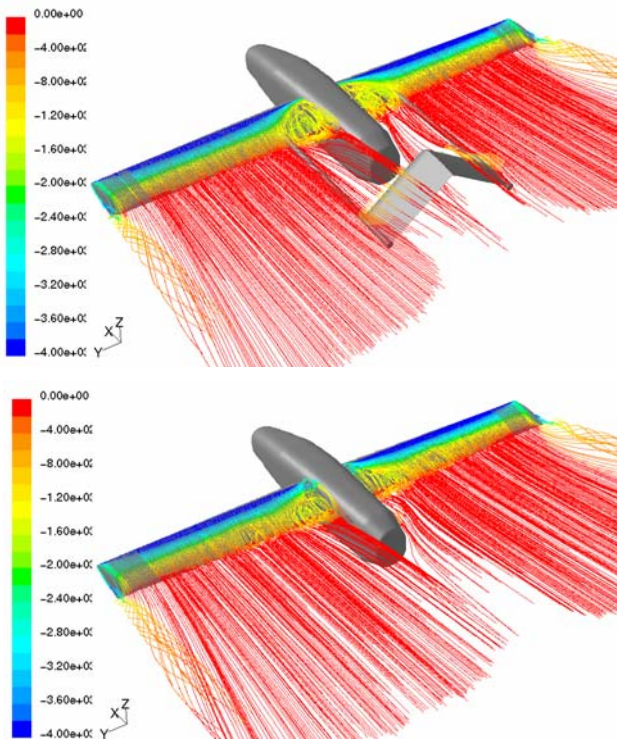
3.3 The Dynamics of the Flow

Shown in Figure 8, the complexity of separation flow patterns can be visualized at the angle of attack beyond

15 degree. For cruise speed, at zero degree of incidence, the flow is quasi-steady and mostly attached over the wing span. The tip vortices is indicated at the both end of the wing. The size of wing tip vortices become larger and larger as the angle of attack was increased. The separation zones become large and dominate at the intersection between wing and fuselage. With the tail installation (model 1), the separation zone is clearly enlarged.



(b) 15 degree of incidence, stall angle

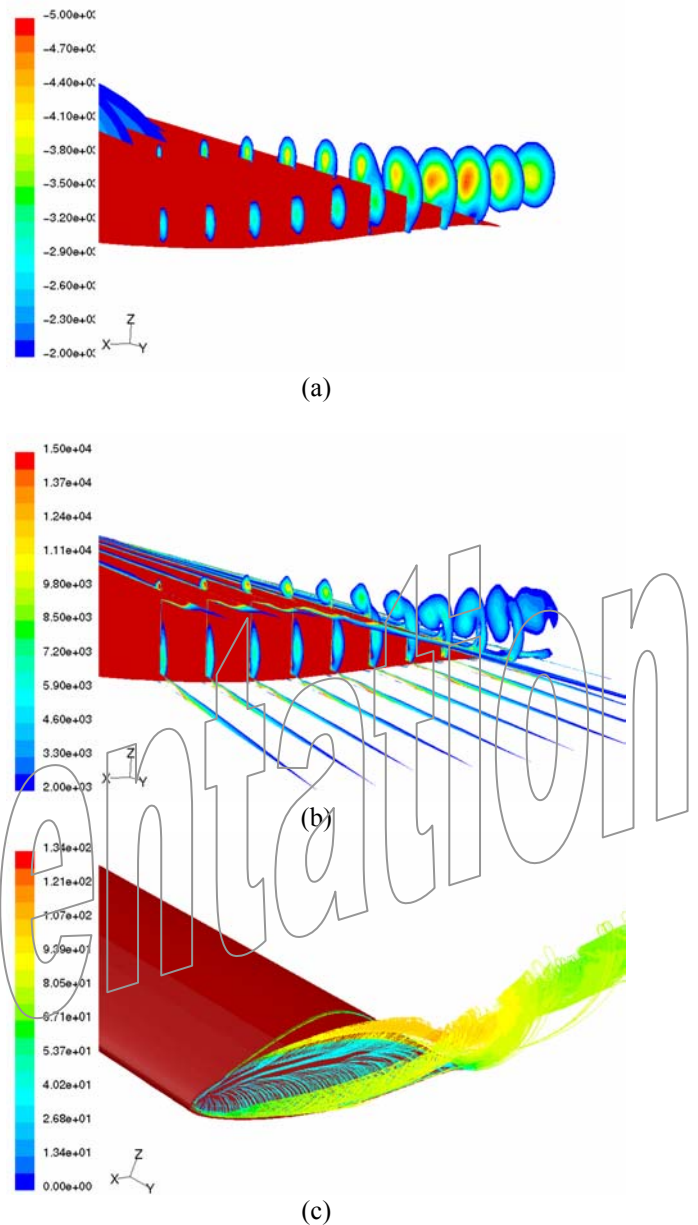


(c) 16 degree of incidence

Figure 8. The path line display at (a) cruise speed, (b) stall angle, and (c) 16 degree of incidence

The wing tip vortices play the major role in aircraft aerodynamics. They are responsible to the induced drag and noise production. The latter become more and more important. Otherwise, they can be harmful to the following aircraft and cause of the traffic delay at the airport.

In reality, the trailing vortices are generated from the pressure difference between upper and lower surfaces and the edges of wing. The pressure driven flows are roll up at the edge of the wing and form as the streamwise vortices. Astonishingly, the detailed structural vortices are quite complicated as shown in Figure 9. At the tip of the wing, the two vertical flows were established at the lower and upper edges of the wing. As the vortices advance downstream, the lower vortices gradually moves up. Ultimately, it reaches the upper edge. The interaction between them befalls. The two vortices coalesce into the single one and travel along the wing upper side until it sheds from the wing surface. The vortices are characterized by the low pressure and high vorticity at their cores. As they progress downstream, the pressure is recovered and their strengths are weakened, depicted in Figure 9 (a) and Figure 9 (b). As seen in Figure 9 (c), the velocities of upper and lower corner streamwise vortices are approximately 1.5 and 1.15 times of the free stream velocity, respectively.



(a)

(b)

(c)

Figure 9. The visualization of the tip vortices (a) the pressure contour, (b) the vorticity contour, and (c) the path line

4. Conclusions and Recommendations

The procedure of Computational Fluid Dynamics or CFD was exploited to establish insight into the nature of the flow over UAV configurations and to investigate the influence of UAV components, including the wing, tail, and fuselage. The $k-\omega$ turbulent models with QUICK numerical scheme have been chosen and implemented on the tetrahedrons.

The installation of the tail caused the slight reduction of drag and lift. From the visualization, the size of wake region in model 1 was enlarged and the size of tip vortices depended on the degree of incidences. Breaking down the lift and drag coefficients for each components, it shown that the wing is mainly represented all

aerodynamic loads. The drop of lift coefficients is consistent with the appearance of the flow separation. In addition, the nature of wing tip vortices was thoroughly explained. The side vortices merged and moved on the upper edge until they came off the wing surface.

In this research, we went deep into the details of each component and their intersection. Nevertheless, due to inadequacy of the computer resource, the present grid distribution has a low quality to efficiently capture some complex phenomenon. Further research that should be performed is the investigation of the mesh refinement to assess the steady desired solutions and ensure the accurate solutions. Also the other necessary flight conditions such as landing, taking off or unsymmetrical flight need to be assessed.

Acknowledgement

The author team wishes to thank the Thailand Research Fund (TRF) and the Defense Research and Development Office (DRDO) for supporting the grant for the research.

References,

- [1] R. Rudnik, S. Melber, A. Ronzheimer, and O. Brodersen. Three-Dimensional Navier-Stokes Simulations for Transport Aircraft High-Life Configurations. *Journal of Aircraft*, Vol. 38, No. 5, September-October 2001.
- [2] Stuart E. Rogers, K. Roth, Hoa V. Cao, Steven M. Nash, and M. David Baker. Computation of Viscous Flow for Boeing 777 Aircraft in Landing Configurations. *Journal of Aircraft*, Vol. 38, No. 6, November-December 2001.
- [3] T. Fujita, Y. Ito, K. Nakahashi, and T. Iwamiya. Computational Fluid Dynamics Evaluation of National Aerospace Laboratory Experimental Supersonic Airplane in Ascent. *Journal of Aircraft*, Vol. 39, No.2, March-April 2002.
- [4] R. Rudnik, Cord-Christian Rossow, Heiko Frhr. V. Geyr. Numerical Simulation of Engine/Airframe Integration for High-bypass Engines. *Aerospace Science and Technology* 6 (2002) 31-42 .
- [5] Fluent Incorporated. *Fluent 6.0 user's guide*. 2001.